Potential Influences of Neglecting Aerosol Effects on the NCEP GFS Precipitation Forecast

Mengjiao Jiang[1,2], Jinqin Feng[3], Zhanqing Li[1,2*], Ruiyu Sun[4], Yu-Tai Hou[4], Yuejian Zhu[4], Bingcheng Wan[5], Jianping Guo[6], Maureen Cribb[2]

1, State Key Laboratory of Earth Surface Processes and Resource Ecology, College of Global Change and Earth System Science, Beijing Normal University, Beijing, China

2, Department of Atmospheric and Oceanic Science and ESSIC, University of Maryland, College Park, Maryland, USA

3, Longyan Meteorological Office of Fujian Province, Longyan, Fujian, China

4, Environmental Modeling Center, National Centers for Environmental Prediction, National Oceanic and Atmospheric Administration, USA

5, State Key Laboratory of Atmospheric Boundary Layer Physics and Atmospheric Chemistry, Institute of Atmospheric Physics, Chinese Academy of Sciences, Beijing, China

6, State Key Laboratory of Severe Weather, Chinese Academy of Meteorological Sciences, Beijing, China

Correspondence to:

Z. Li,

zhanqing@umd.edu

Abstract

Aerosol-cloud interactions (ACI) have been widely recognized as a factor affecting precipitation. However, they have not been considered in the operational National Centers for Environmental Predictions Global Forecast System model. We evaluated the potential impact of neglecting ACI on the operational rainfall forecast using ground-based and satellite observations, and model reanalysis. The Climate Prediction Center unified gauge-based precipitation analysis and the Modern-Era Retrospective analysis for Research and Applications Version 2 aerosol reanalysis were used to evaluate the forecast in three countries for the year 2015. The overestimation of light rain (47.84%) and underestimation of heavier rain (31.83%, 52.94%, and 65.74% for moderate rain, heavy rain, and very heavy rain, respectively) from the model are qualitatively consistent with the potential errors arising from not accounting for ACI, although other factors cannot be totally ruled out. The standard deviation of the forecast bias was significantly correlated with aerosol optical depth in Australia, the U.S., and China. To gain further insight, we chose the province of Fujian in China to pursue a more insightful investigation using a suite of variables from gauge-based observations of precipitation, visibility, water vapor, convective available potential energy (CAPE), and satellite datasets. Similar forecast biases were found: over-forecasted light rain and under-forecasted heavy rain. Long-term analyses revealed an increasing trend of heavy rain in summer, and a decreasing trend of light rain in other seasons, accompanied by a decreasing trend in visibility, no trend in water vapor, and a slight increasing trend in summertime CAPE. More aerosols

45   decreased cloud effective radii for cases where the liquid water path was greater than

46   100 g m^{-2}. All findings are consistent with the effects of ACI, i.e., where aerosols

47   inhibit the development of shallow liquid clouds and invigorate warm-base

48   mixed-phase clouds (especially in summertime), which in turn affects precipitation.

49   While we cannot establish rigorous causal relations based on the analyses presented in

50   this study, the significant rainfall forecast bias seen in operational weather forecast

51   model simulations warrants consideration in future model improvements.

1. Introduction

Aerosols affect precipitation by acting as cloud condensation nuclei (CCN) and ice nuclei (IN), which can influence cloud microphysics (Twomey et al., 1984) and cloud lifetime (Albrecht, 1989). By absorbing and scattering radiation in the atmosphere, aerosols can alter the thermal and dynamic conditions of the atmosphere. The two types of effects are broadly referred to as aerosol-cloud interactions (ACI) and aerosol-radiation interactions (ARI) (Intergovernmental Panel on Climate Change, 2013). Both can influence precipitation (Rosenfeld et al., 2008) and many other meteorological variables to the extent that they may account for the considerable changes in climate experienced in Asia over the past half century (Li et al., 2016).

The impact of aerosols on precipitation via cloud microphysics occurs through warm-rain and cold-rain processes, as reviewed by Tao et al. (2012). In the warm-rain process, the competition for water vapor leads to a greater number of cloud drops with smaller sizes as the aerosol loading increases. This decreases the collision efficiency because of the low fall speed and low droplet-collecting efficiency. Rain formation is thus slowed down. Also, a heavier aerosol loading narrows the cloud drop-size spectrum, lowering the coalescence and collision efficiencies. The delay in precipitation formation from the warm-rain process enhances condensation and freezing, and ultimately, leads to the release of extra latent heat above the $0^{o}C$ isotherm (Andreae et al., 2004; Rosenfeld et al., 2008), favoring mixed-phase and cold rainfall processes. ARI also affect precipitation. First, solar radiation absorbed by aerosols may warm up a cloud droplet enough to evaporate it (Ackerman et al., 2000).

74 Second, heating of an aerosol layer due to absorption and cooling of the surface

75 because of the reduction in radiation reaching the ground stabilizes the lower

76 boundary-layer atmosphere and suppresses the formation and development of low

77 clouds whose occurrence decreases with increasing aerosol loading (Li et al., 2011).

78 The suppressed convection by ARI may also lead to rainfall enhancement downwind

79 of polluted places (Carrió et al., 2010; Fan et al., 2015). The combination of ARI and

80 ACI leads to a non-monotonic response of rainfall to aerosols: increasing first and

81 then decreasing (Jiang et al., 2016) because the ACI and ARI are most significant for

82 low and high aerosol loadings, respectively (Rosenfeld et al., 2008; Koren et al., 2008;

83 Fan et al., 2016).

84   Most findings concerning the aerosol suppression of clouds and precipitation are

85 associated with stratocumulus clouds, cumulus clouds, and shallow convection

86 (Albrecht, 1989; Rosenfeld, 2000; Jiang et al., 2006; Xue & Feingold, 2006; Khain et

87 al., 2008), whereas those of enhanced rainfall are associated with deep convective

88 clouds (Koren et al., 2005; Lin et al., 2006; Bell et al., 2008; Rosenfeld et al., 2008).

89 Li et al. (2011) used 10 years of ground-based observations to examine the long-term

90 impact of aerosols on precipitation and found rainfall enhancement in mixed-phase

91 warm-base clouds and suppression in liquid clouds. Van den Heever et al. (2011)

92 underlined the importance of cloud type in dealing with the impact of aerosols on

93 precipitation.

94   Forecasting rainfall is most challenging and important in numerical weather

95 prediction (NWP). In the current Global Forecast System (GFS) model, aerosols are

96   only considered in the radiation scheme on a climatological scale. ARI are only

97   considered offline and are not coupled with the dynamic system. ACI have not yet

98   been accounted for. To improve the forecast accuracy, a suite of new physical schemes

99   are being implemented in the National Centers for Environmental Prediction

100   (NCEP)'s Next-Generation Global Prediction System. The goal of modifying the

101   current forecast model is to improve physical parameterizations in such a way that

102   allows for efficient, accurate, and more complete representations of physical

103   processes and their interactions including at least some of the aforementioned aerosol

104   mechanisms.

105   As a first step, the goal of the present study is to evaluate current operational

106   GFS forecast results (before any ACI are introduced) to see if any systematic

107   precipitation biases bear resemblance to aerosol perturbations. A gross evaluation of

108   the GFS model forecast results in three countries (China, the U.S., and Australia) were

109   chosen because they cover all hemispheres and represent different atmospheric and

110   environmental conditions. Moreover, there are the U.S. Department of Energy's

111   Atmospheric Radiation Measurement (ARM) observations in all three countries that

112   will be used in follow-on studies to gain a deeper insight into causal relationships and

113   the impact of different parameterization schemes. Descriptions of the operational GFS

114   model, datasets, and the evaluation strategy and statistical method used are presented

115   in section 2. Results of the evaluation and possible explanations are given in section 3.

116   A summary of the research and discussion are given in Section 4.

117

2. Model, Datasets, and Methodology

2.1 Description of the NCEP GFS Model

The NCEP GFS model is a global spectral forecast model (spherical harmonic basis functions) that has been described and evaluated over the years (e.g., Kanamitsu, 1989; Yang et al., 2006; Sela, 2009; Yoo et al., 2012, 2013). Shortwave and longwave radiation are parameterized using the Rapid Radiative Transfer Models (RRTMG) RRTMG_SW (v3.8) and RRTMG_LW (updated based on AER's version 4.8), respectively, developed at AER Inc. (http://www.emc.ncep.noaa.gov/GFS/doc.php). A monthly climatology of aerosols composed of five primary species similar to those in the Goddard Chemistry Aerosol Radiation and Transport model (GOCART; Chin et al., 2002) was used. One or two major components in each grid (based on climatology) were chosen for both longwave and shortwave radiative transfer calculations. In the planetary boundary layer (PBL), a hybrid eddy-diffusivity mass flux PBL parameterization (Han et al., 2016) was incorporated to replace the previous PBL scheme (Troen & Mahrt, 1986; Hong & Pan, 1996). A modified version (Han & Pan, 2011) of the Simplified Arakawa-Schubert scheme (Arakawa & Schubert, 1974; Grell, 1993; Pan & Wu, 1995) is used for deep convection in the GFS model. The new shallow convection scheme (Han & Pan, 2011) uses a bulk mass-flux parameterization, which is similar to the deep convection scheme, but with a cloud-top limit of 700 hPa and different specifications on entrainment, detrainment, and mass flux at the cloud base. A prognostic cloud water scheme (Sundqvist et al.,

140 1989; Zhao & Carr, 1997; Moorthi et al., 2001) was added in May 2001. Grid-scale

141 precipitation is the sink of cloud condensate and is diagnostically calculated from

142 cloud condensate. It is parameterized following Zhao & Carr (1997) for ice (snow),

143 evaporation of rain and snow, and the melting of snow, and following Sundvist et al.

144 (1989) for liquid water (rain) (GCWM Branch, EMC, 2003).

145

146 **2.2 Descriptions of Datasets Used**

147   Datasets used include Modern-Era Retrospective analysis for Research and

148 Applications Version 2 (MERRA-2) aerosol optical depth (AOD) data, Climate

149 Prediction Center (CPC) unified gauge-based precipitation data, and the NCEP GFS

150 precipitation forecast data for the year 2015 in three countries: China, the U.S., and

151 Australia. Other datasets used include long-term NCEP Global Ensemble Forecast

152 System (GEFS) precipitation forecast data, ground-based observations of precipitation

153 and visibility, water vapor and convective available potential energy (CAPE)

154 sounding datasets, and satellite-retrieved aerosol and cloud properties for a small

155 region of Fujian Province in China chosen for more detailed study.

156 **2.2.1 NASA MERRA-2 Aerosol Reanalysis**

157   The MERRA-2 aerosol reanalysis (Randles et al., 2016) is an upgrade of the

158 off-line aerosol reanalysis called MERRAero (da Silva et al., 2011; Rienecker et al.,

159 2011; Jiang et al., 2016). The aerosol module in MERRAero is based on the

160 GOCART model (Chin et al., 2002). The AOD observing system sensors extend from

161 the Moderate Resolution Imaging Spectroradiometer (MODIS) Neural Net Retrieval

162   (NNR) in MERRAero to a combination of the Advanced Very-High-Resolution

163   Radiometer NNR, Aerosol Robotic Network, the Multi-angle Imaging

164   SpectroRadiometer, the MODIS/Terra NNR, and the MODIS/Aqua NNR in the

165   MERRA-2 aerosol reanalysis. More details about the MERRA-2 aerosol reanalysis

166   can be found in Randles et al. (2016). Hourly total aerosol extinction AOD data at 550

167   nm at a resolution of $0.625\,°$ x $0.5\,°$ for the year 2015 are used in this study.

168   **2.2.2 CPC Unified Gauge-based Analysis of Global Daily Precipitation**

169   A unified suite of precipitation analysis products that ingest a gauge-based

170   analysis of global daily precipitation over land were assembled at NOAA's CPC

171   (https://climatedataguide.ucar.edu/climate-data/cpc-unified-gauge-based-analysis-glob

172   al-daily-precipitation). Over 17,000 station reports were first collected from multiple

173   sources. Quality control was performed through comparisons with other sources of

174   data, e.g., from radar, satellite, numerical models, independent nearby stations, and

175   historical precipitation records. Post-quality control corrected reports are interpolated

176   to create the analyzed fields. Orographic effects are considered in this step (Xie et al.,

177   2007). Finally, the daily analysis is constructed and released at a 0.5^{o} x 0.5^{o} resolution

178   (https://climatedataguide.ucar.edu/climate-data/cpc-unified-gauge-based-analysis-glob

179   al-daily-precipitation). Daily precipitation data for the year 2015 are used in this

180   study.

181   **2.2.3 NCEP GFS/GEFS Forecast Datasets**

182   NWP model forecast data used are three-hourly rainfall forecasts from the NCEP

183   GFS model initialized at 00 coordinated universal time (UTC) and accumulated for 24

184   hours in the three countries chosen for study. The relative humidity (RH) at 850 hPa

185   and the liquid water path (LWP) calculated following Yoo et al. (2012) are used,

186   corresponding to the precipitation record in the three countries at a 0.5^ox0.5^o

187   latitude-longitude resolution. For the part of the study focused on Fujian Province,

188   China, the long-term NWP model reforecast precipitation amount accumulated over

189   the period of 12 hours to 36 hours out from 00 UTC at a 1^ox1^o latitude-longitude

190   resolution for the years 1985 to 2010 are used.

191   **2.2.4 Long-term Ground-based Observations in Fujian Province, China**

192   Ground meteorological data acquired in Fujian Province from 1980 to 2009 are

193   used in this study. Figure 1 shows the locations of the 67 meteorological stations

194   measuring precipitation. Sixteen of these stations also collect visibility data four times

195   a day. Daily mean data are used here. Visibility has been used as proxy for aerosol

196   loading in China in several studies (Rosenfeld et al., 2007; Yang et al., 2013; Yang &

197   Li, 2014). The main advantage is the long measurement record under all sky

198   conditions. However, there are some limitations, e.g., the uncertainty due to humans

199   making the observations and the influence of aerosol hygroscopic growth. To remove

200   the humidity influence on visibility, visibility was corrected for RH (Charlson, 1969;

201   Appel et al., 1985) using the formula adopted by Rosenfeld et al. (2007) when RH

202   falls between 40% and 99%:

203
$$\frac{V_{ori}}{V_{cor}} = 0.26 + 0.4285 \, lg(100 - RH), \qquad (1)$$

204   where RH is in percent, and $V_{ori} \, and \, V_{cor}$ are the originally uncorrected and

205   corrected visibilities, respectively. Only non-rainy data were used.

206   To analyze water vapor and atmospheric stability effects on precipitation, data

207 collected twice a day (at 00 UTC and 12 UTC) from three atmospheric sounding

208 stations (Xiamen, 24.48^{o}N, 118.08^{o}E; Shaowu, 27.33 N, 117.46 E; Fuzhou, 26.08^{o}N,

209 119.28^{o}E) are used to calculate trends in precipitable water vapor and CAPE. Daily

210 precipitable water and CAPE values are the mean of the two measurements made per

211 day.

212 **2.2.5 Satellite Datasets of Aerosol and Cloud Properties in Fujian Province,**

213 **China**

214   CloudSat data from 2006–2010 amassed over Fujian Province (22.5^{o}N-28.5^{o}N,

215 114.5^{o}E-120.5^{o}E) are used to extract cloud-top and cloud-base height information.

216 CloudSat retrievals of cloud-top and base heights are converted to temperatures using

217 temperature profiles from the European Center for Medium-range Weather

218 Forecasting Auxiliary product. The converted cloud-top and cloud-base temperatures

219 are used for cloud type classification. The classification of different cloud types is

220 summarized in Table 1 and introduced in sub-section 2.3.2. Only single-layer clouds

221 detected by the CloudSat are chosen here.

222   Aqua/MODIS retrievals of cloud droplet size and LWP for liquid clouds (clouds

223 with cloud-top temperatures (CTT) greater than 273 K) collected over Fujian

224 Province from 2003–2012 are used. Errors in satellite retrievals of AOD such as

225 cloud contamination (Kaufman et al., 2005; Zhang et al., 2005) introduce

226 uncertainties in the aerosol-cloud relationship (Gryspeerdt et al., 2014a, b). We use

227 MODIS Level 3 AOD with AOD > 0.6 excluded and not the higher resolution Level 2

228   product to reduce the possibility of cloud contamination (Niu and Li, 2012) in AOD

229   retrievals.

230

231   **2.3 Methodology**

232

233   **2.3.1 Spatial and Temporal Matching of Model and Observation Data**

234   CPC-unified gauge-based daily precipitation data at a 0.5^o x 0.5^o

235   latitude-longitude resolution in the three countries for the year 2015 are used. GFS

236   model grid 004 data at the same latitude-longitude resolution (0.5^o x 0.5^o) are also

237   used. Forecast precipitation for a one-day accumulation generated at three-hourly

238   intervals (e.g., at 03, 06, 09, 12, 15, 18, 21, 24 UTC), starting from the control time of

239   00 UTC, are used to match the corresponding gauge-based observations. The

240   MERRA-2 aerosol analysis is not coupled with GFS simulations. Daily MERRA-2

241   AOD is at a resolution of 0.625^o x 0.5^o and is interpolated to the CPC and GFS

242   precipitation resolution using a linear interpolation method. The spatial and temporal

243   resolutions of the matched data sets are $0.5^{\,o}$ x $0.5^{\,o}$ and are generated for each day.

244   There are ~3 686 000 grid points in total.

245   For the long-term analysis focused on Fujian, China, the NWP model reforecast

246   precipitation amount accumulated over the period of 12 hours to 36 hours out from

247   the 00 UTC run at six-hourly intervals and at a 1° x 1° latitude-longitude resolution for

248   the years 1985 to 2010 are used to calculate the modeled daily precipitation amount in

249   each grid box. They are interpolated to match the long-term ground-based

250   precipitation observations recorded at each of the 67 stations in the study region of

251   Fujian, China (Fig. 1). There are 9495 days in total with matched data.

252   **2.3.2 Rainfall Level Classification and Cloud Type Classification**

253   Based on the definitions of the China Meteorological Administration,

254   precipitation data are classified into four groups according to the daily rain amount:

255   light rain (0.1–9.9 mm d^{-1}), moderate rain (10–24.9 mm d^{-1}), heavy rain (25–49.9 mm

256   d^{-1}), and very heavy rain ($\geq$ 50 mm d^{-1}). Rain gauge data are usually used as reference

257   data in weather forecast and model evaluations because they come from direct

258   physical records (Tapiador et al., 2012). The most commonly-used rain detector is the

259   tipping bucket. Once the bucket is filled (0.1 mm), the bucket is emptied and produces

260   a signal. This process repeats until precipitation stops. Light rain less than 0.1 mm

261   cannot be measured. Therefore, the definition of light rain is 0.1–9.9 mm d^{-1}.

262   Table 1 summarizes the cloud types considered in the Fujian Province analysis.

263   Deep mixed-phase clouds are defined as clouds with cloud-base temperatures (CBT) >

264   15°C and CTT < -4°C, shallow mixed-phase clouds are defined as clouds with CBT

265   ranging from 0°C to 15°C and CTT < -4°C, and pure liquid clouds are defined as

266   clouds with CBT > 0°C and CTT > 0°C (Li et al., 2011; Niu & Li, 2012).

267   **2.3.3 Evaluation Methods**

268   Quantitative precipitation forecast scores developed by NCEP are used in the

269   evaluation. Table 2 is a contingency table based on documents from the World

270   Climate   Research   Programme

271   (http://www.cawcr.gov.au/projects/verification/#Methods_for_dichotomous_forecasts

272   ). The most commonly-used statistical scores are the equitable threat score (ETS),

273   which is also called the Gilbert skill score, and the bias score (BIAS). The ETS is

274   given by

275     $$ETS = \frac{H - H_{random}}{H + m + f - H_{random}},\qquad\qquad(2)$$

276   where H represents hits, f represents false alarms, and m represents misses. H_{random}

277   is given by

278     $$H_{random} = \frac{(H + m) * (H + f)}{TOTAL}.\qquad\qquad(3)$$

279   Its values range from -1/3 to 1 and a perfect score is 1. The BIAS is expressed as

280     $$BIAS = \frac{H + f}{H + m}.\qquad\qquad(4)$$

281   Its values range from 0 to infinity. A perfect score is 1. A BIAS $<$ 1 indicates

282   under-forecasting and a BIAS $>$ 1 indicates over-forecasting.

283   Under limited ranges of LWP or RH, the top and bottom one-third of AOD

284   values denote polluted and clean subsets of data. To obtain the forecast skill under a

285   particular pollution condition, the ETS and the BIAS for clean and polluted conditions

286   are calculated as

287     $$< ETS >_{i,j,m} = (ETS)_{i,j,m},\qquad\qquad(5)$$

288     $$< BIAS >_{i,j,m} = (BIAS)_{i,j,m},\qquad\qquad(6)$$

289   for the index of precipitation threshold (i), RH or LWP (j), and clean or polluted

290   scenario (m).

291   **2.3.4 Statistical Method**

292   The standard deviation of the precipitation bias between the GFS model and CPC

293   gauge data is calculated as

294
$$S = \sqrt{\frac{\sum(x-r)^2}{n-1}} \, , \qquad\qquad (7)$$

295 where x is the forecast bias on a single day, n is equal to 364 days, and r is the mean

296 forecast bias. Pearson's method is used to calculate the linear correlation coefficient of

297 the relationship between the standard deviation of the forecast difference and AOD. A

298 t-test is applied with the p value set to 0.05.

299   The relative difference between the forecast precipitation and observations is

300 calculated as

301
$$\Delta P = \frac{P_{GFS/GEFS} - P_{OBV}}{P_{OBV}} \times 100\%, \qquad\qquad (8)$$

302 where $P_{GFS/GEFS}$ refers to the forecast precipitation and P_{OBV} refers to the

303 precipitation from gauge-based observations.

304   For the long-term analysis, trends in a particular parameter are defined as the

305 relative change in the parameter (in %) over each successive decade (Lin & Zhao,

306 2009). The Mann-Kendall method is used to test the significance of the trend.

307

308 **3. Results**

309

310 **3.1 Evaluation of GFS Precipitation using the CPC Gauge-based Analysis**

311

312 **3.1.1 Annual Mean Patterns**

313   The CPC gauge-based precipitation analysis from 2015 is used to evaluate the

314 GFS precipitation forecast. Figure 2 shows the annual mean precipitation difference

315 between the GFS model and the CPC analysis for three countries, i.e., China, the U.S.,

and Australia, for the year 2015. Values above (below) zero represent the overestimation (underestimation) of precipitation. In China (Figure 2a), the GFS model overestimates the mean daily rainfall mostly in southwest China, especially in Sichuan, Yunnan, and Guizhou Provinces (by ~3 mm d^{-1}), and in northwest China where rain events are scarcer. Rainfall is underestimated over the Yangtze River Delta region and the eastern coast of China. In the U.S. (Figure 2b), the GFS model overestimates precipitation by about 1–2 mm d^{-1} in most regions and underestimates precipitation along the coastline of the Gulf of Mexico (by ~1 mm d^{-1}). In Australia (Figure 2c), the forecast performance is good. In northern Australia, the underestimation of precipitation is around 2 mm d^{-1}. Z-scores were calculated to test the significance of the annual mean difference in the daily rainfall amount between the GFS model forecast and the CPC analysis. Z values range from -0.4803 to 0.8534 over the grids in the three countries. Because the Z-score values are less than 2, this indicates that the mean difference is not significant at the two-sigma level. Therefore, the forecast performance of the GFS model with regard to the annual mean daily rainfall in the three countries is sound with reference to the gauge-based CPC rainfall analysis.

3.1.2 Different Rainfall Intensities

Figure 3 shows the annual mean relative difference between forecast precipitation and observations for light rain (0.1–10 mm d^{-1}) and heavier rain (> 10 mm d^{-1}). The GFS model overestimates light rain in most places (Figure 3a) and underestimates heavier rain (Figure 3b). This suggests that both the overestimation of

light rain and underestimation of moderate rain, heavy rain, and very heavy rain

contribute to the forecast bias. Figure 4 shows the mean relative difference between

forecast and observed daily precipitation amounts for different rain intensities in the

three countries for the whole year (Fig. 4a) and for summer only (Fig. 4b). GFS

forecasts overestimate light rain by 47.84% and underestimate moderate rain, heavy

rain, and very heavy rain by 31.83%, 52.94%, and 65.74%, respectively (Fig. 4a). The

underestimation of precipitation in summer is larger for moderate rain (32.93%),

heavy rain (55.19%), and very heavy rain (66.93%, Fig. 4b). These model biases are

caused by many factors that are beyond the scope of this paper to examine. Our focus

is on any potential contribution of neglecting aerosol effects to the biases. The

relationship between model performance and AOD is thus further investigated.

3.1.3 Relationship between Model Performance and AOD

In principle, the underestimation and overestimation at different rainfall levels

(Figs. 3 and 4) may be linked to AOD conditions, as elaborated in the introduction of

previous studies (c.f. the review of Tao et al., 2012). The standard deviation of the

forecast bias at each grid point in the three countries is calculated to further examine

the links between the model bias and AOD. Aerosols tend to polarize precipitation by

suppressing light rain and enhancing heavy rain, and thus increase the standard

deviation. The calculation of the standard deviation of the forecast difference is based

on Eqn. (7). Figure 5 shows the relationship between the standard deviation and AOD

in the three countries. Each point represents a grid box. The standard deviation and

AOD has a significant positive correlation in the three countries with correlation

360 coefficients of 0.5602, 0.6522, and 0.5182 for Australia, the U.S., and China,

361 respectively. This suggests that the degree of disparity of the forecast error is larger

362 for grids with high aerosol loading. The slopes of the best-fit lines are 75.23 for

363 relatively clean Australia (maximum AOD < 0.18), 48.4 for the polluted U.S.

364 (maximum AOD < 0.20), and 8.554 for heavily polluted China (maximum AOD >

365 0.60).

366  The ETS and BIAS are used to examine the model performance under clean and

367 polluted conditions for different AOD bins with fixed LWP (Figs. 6a and 6c) or RH

368 (Figs. 6b and 6d) in the three countries. For a particular LWP or RH condition, the top

369 and bottom one-third of AOD values are defined as polluted and clean subsets of data.

370 In Figs. 6a and 6b, ETS increases as the LWP or RH increases. This is because

371 large-scale precipitation is diagnosed from cloud mixing ratios. The ETS are smaller

372 for the polluted scenario than for the clean scenario, especially under high LWP or

373 high RH conditions. In Figs. 6c and 6d, the BIAS decreases under polluted conditions

374 compared with the BIAS under clean conditions. The decreases in ETS and BIAS

375 under polluted conditions suggest that AOD influences the model rainfall forecast.

376

377 **3.2 Potential Contribution of Aerosols to the Model Bias**

378

379 **3.2.1 Long-term Forecast Bias and Trends in Observed Precipitation in Fujian**

380 **Province, China**

381  The model performance differs under different conditions, e.g., initial and

dynamic settings, and weather regimes. A long-term statistical evaluation of rainfall

forecasts for Fujian Province is made to mitigate these fluctuations in the model

forecast accuracy. Model data from 1985 to 2010 are used to calculate the relative

difference based on Eqn. (8). Figure 7 shows the mean relative difference between

forecast and observed precipitation for different rain rates from the 67 stations in

Fujian Province for all seasons and for summer only. Figure 7a shows that there is

114.36% more precipitation forecast by the NCEP/GEFS model than observed for the

light rain cases. For moderate rain, heavy rain, and very heavy rain cases, 29.20%,

41.74%, and 59.30% less precipitation than observed, respectively, was forecast. The

underestimation of moderate rain (46.88%), heavy rain (59.58%), and very heavy rain

(70.16%) is even larger in summer (Fig. 7b).

Seasonally-averaged trends (percent change per decade) in daily rain amount and

frequency over Fujian Province from 1980 to 2009 are calculated. Only the results for

rain amount are shown in Fig. 8 because the frequency results bear a close

resemblance. Cross-hatched bars represent data at a confidence level greater than 95%.

In spring, daily rain amounts decreased over time, ranging from -4.9% to -15.3% per

decade for different rain rates. In summer, heavy and very heavy daily rain amounts

increased significantly. For very heavy rain, the amount and frequencies increased at a

rate of 21.8% and 24.5% (not shown), respectively. In autumn, light rain and

moderate rain amounts decreased. In winter, the light rain amount decreased over time.

Decreases in light rain amounts are -8.4% per decade. Overall, the increasing trends in

summertime for heavy and very heavy rain are most significant. The decreasing

404   trends in light rain in other seasons are also significant.

405   **3.2.2 Examination of Potential Contributors**

406   Reasons for the difference between modeled and observed precipitation are

407   examined in terms of aerosol effects, water vapor, and CAPE. Time series of visibility

408   over the period of 1980–2009 are shown in Fig. 9. Visibility has declined steadily in

409   all seasons but summer during which there was a short-lived increasing trend from

410   1992–1997. The linear declining trends are statistically significant at the 95%

411   confidence level. The greatest reduction is seen during the summer, especially after

412   1997. Tables 3 and 4 summarize the correlation between visibility and precipitation

413   amount and frequency, respectively. A positive (negative) correlation between

414   visibility and precipitation means a negative (positive) correlation between aerosol

415   concentration and precipitation. Values with an asterisk represent data at a confidence

416   level greater than 95%. For light rain, the correlations between daily rain amount and

417   visibility (Table 3) and between rain frequency and visibility (Table 4) are positive for

418   all seasons. For heavy rain to very heavy rain, the correlations between visibility and

419   daily rain amount (Table 3), as well as frequency (Table 4), are negative in summer.

420   The water vapor amount and atmospheric stability are important factors related

421   to precipitation. To analyze the potential contributions of these factors to the forecast

422   bias, their effects on precipitation are examined. Data from three atmospheric

423   sounding stations (Xiamen, 24.48^{o}N, 118.08^{o}E; Shaowu, 27.33^{o}N, 117.46^{o}E; Fuzhou,

424   26.08^{o}N, 119.28^{o}E) collected from 1980–2009 are used to calculate trends in

425   precipitable water vapor and CAPE. Figure 10 shows time series of annual mean

426   water vapor amount for different seasons. A slight increasing trend is seen in winter,

427   while no discernible trend is seen in other seasons. This suggests that the water vapor

428   amount characterizing the study region cannot explain seasonal variations in

429   precipitation. Time series of mean CAPE for the different seasons are shown in Fig.

430   11. There is an increasing trend in summertime CAPE during the period of 1980–2009,

431   but the trends are not as strong in other seasons. The observed increase in rain amount

432   in summer is in part likely due to an increase in convective precipitation events that

433   arises from the increasing trend in CAPE.

434   **3.2.3 Impact of Aerosols on Clouds and Precipitation**

435   Aerosols can influence precipitation through warm- and cold-rain processes (Tao

436   et al., 2012). Cloud droplet size, LWP for clouds with CTT greater than 273 K, and

437   AOD at 550 nm retrieved from the Aqua/MODIS platform over Fujian Province

438   during the period of 2003–2012 are used to examine the impact of aerosols on cloud

439   effective radius (CER). Figure 12 shows CER as a function of AOD for liquid clouds

440   with different LWPs. When the AOD is small (< 0.2), the CER increases with

441   increasing LWP. For LWP > 100 g m^{-2}, the CER decreases with increasing AOD,

442   which suggests that more aerosols decrease CERs. This result is in line with the two

443   aerosol indirect effects (Twomey et al., 1984; Albrecht, 1989). A greater number of

444   smaller droplets may reduce the precipitation efficiency and suppress or enhance

445   precipitation, as reviewed by Tao et al. (2012).

446   Several observational and model studies suggest that smaller cloud particles are

447   more likely to ascend to above the freezing level, releasing latent heat and

448   invigorating deep convection (Rosenfeld et al., 2008; Li et al., 2011) while

449   suppressing shallow convection. CTTs and CBTs, converted from CloudSat

450   measurements of cloud top and base heights, in Fujian Province from 2006 to 2010

451   are used to study the impact of aerosols on the cloud development of different clouds.

452   Figure 13 shows CTT as a function of AOD for liquid and warm- and cold-base

453   mixed-phase clouds. Definitions of the different cloud types are summarized in Table

454   1, which is taken from Li et al. (2011). Left-hand ordinates are for liquid clouds, while

455   right-hand ordinates are for warm-base and cold-base mixed-phase clouds. For all

456   seasons (Fig. 13a), CTTs of warm-base mixed-phase clouds are lower than those of

457   cold-base mixed-phase clouds. Warm-base mixed-phase CTTs decrease with

458   increasing AOD, which indicates that cloud-top heights have increased. For cold-base

459   mixed-phase clouds, variations in CTT with AOD are not obvious. For liquid clouds,

460   CTTs increase slightly with AOD, which means that the development of liquid clouds

461   is suppressed when AOD increases. The negative slope of the linear relationship

462   between CTT and AOD for warm-base mixed-phase clouds and the positive slope of

463   the linear relationship between CTT and AOD for liquid clouds are both stronger in

464   summer (Fig. 13b). This suggests that aerosols inhibit the development of shallow

465   liquid clouds and invigorate warm-base mixed-phase clouds, with little influence on

466   cold-base mixed-phase clouds. These effects of aerosols on summertime cloud

467   development are more obvious, likely because convective clouds occur more

468   frequently during the summertime in Fujian Province.

469   These results agree with those from a ground-based study using ARM Southern

470 Great Plains data (Li et al., 2011) and from tropical region studies using

471 CloudSat/Cloud-Aerosol Lidar and Infrared Pathfinder Satellite Observation data (Niu

472 & Li, 2012; Peng et al., 2016). The impact of aerosols on different types of clouds

473 may lead to light rain suppression and heavier rain enhancement. If the GFS model

474 neglects aerosol effects, overestimations of light rain and underestimations of heavy

475 to very heavy rain may be forecast, especially in summer. For example, Fig. 14 shows

476 time series of regionally-averaged daily modeled and observed precipitation in 2001.

477 Modeled and observed precipitation amounts over the region agree well in spring and

478 winter while modeled precipitation amounts are greater than observations for light

479 rain in autumn. Note that modeled precipitation amounts are significantly less than

480 observed precipitation amounts over the region in summer when deep convective

481 clouds and heavy to very heavy rain tends to occur. Although there are many reasons

482 for the difference between modeled and observed precipitation, these results suggest

483 that to some extent, the neglect of aerosol effects may contribute to the model rainfall

484 forecast bias.

485

486 **4. Summary and Discussion**

487

488 Aerosol-cloud interactions (ACI) have been recognized as playing a vital role in

489 precipitation, but have not been considered in the National Centers for Environmental

490 Prediction (NCEP) Global Forecast System (GFS) model yet. For more efficient and

491 accurate forecasts, new physical schemes are being incorporated into the NCEP's

492 Next-Generation Global Prediction System. As a benchmark evaluation of model

493 results that exclude aerosol effects, the operational precipitation forecast (before any

494 ACI are included) is evaluated using multiple datasets with the goal of determining if

495 there is any link between the model forecast bias and aerosol loading. Multiple

496 datasets are used, including ground-based precipitation and visibility datasets,

497 Aqua/Moderate Resolution Imaging Spectroradiometer products, CloudSat retrievals

498 of cloud-base and cloud-top heights, Modern-Era Retrospective analysis for Research

499 and Applications Version 2 model simulations of aerosol optical depth (AOD), and

500 GFS forecast datasets.

501 Operational daily precipitation forecasts for the year 2015 in three countries, i.e.,

502 Australia, the U.S., and China, were evaluated. The model overestimates light rain,

503 and underestimates moderate rain, heavy rain, and very heavy rain. The

504 underestimation of precipitation in summer is even larger. This is consistent

505 qualitatively with expected results because the model does not account for aerosol

506 effects on precipitation, i.e., the inhibition of light rain and enhancement of heavy rain

507 by aerosols. The standard deviations of forecast differences are generally positively

508 correlated with increasing aerosol loadings in the three countries. Equitable threat

509 scores and BIAS scores decrease for the polluted scenario.

510 An analysis of long-term measurements from Fujian Province, China was done.

511 Light rain overestimation, and moderate, heavy, and very heavy rain underestimations

512 from the Global Ensemble Forecast System were also seen. The underestimation for

513 stronger rainfall was larger in the summertime. Increasing trends for heavy and very

514   heavy rain in summer, and decreasing trends for light rainfall in other seasons were

515   significant from 1980 to 2009. Long-term analyses show that neither water vapor nor

516   convective available potential energy can explain these trends. Satellite datasets

517   amassed in Fujian Province from 2006 to 2010 were used to shed more light on the

518   impact of aerosols on cloud and precipitation. As implied by the Twomey effect, cloud

519   effective radii decrease with increasing AOD, which likely suppresses light rain and

520   enhances heavy rain. This may contribute to the model forecast bias to some extent.

521   The underestimation of heavy rain in summer most likely occurs because deep

522   convective clouds occur more frequently during the summertime in Fujian Province.

523   How neglecting ACI in the operational forecast model impacts model biases remains

524   an open question. This study is arguably the first attempt at evaluating numerical

525   weather prediction forecast errors in terms of the potential effects of aerosols. A more

526   rigorous and systematic evaluation to gain insights into the model is needed. Toward

527   this goal, case-based investigations using rich instantaneous measurements are

528   currently underway.

Data Availability

529

530   Forecast data are from the NOAA NOMADS (https://nomads.ncdc.noaa.gov/)

531 for GFS data (https://nomads.ncdc.noaa.gov/data/gfs4/) and the NOAA NCDC

532 (https://www.ncdc.noaa.gov/data-access/model-data/model-datasets/global-ensemble-

533 forecast-system-gefs) for GEFS reforecast data. NASA MERRA-2 aerosol data are

534 accessible   from   the   NASA   Global   Modeling   and   Assimilation   Office

535 (https://gmao.gsfc.nasa.gov/reanalysis/MERRA-2/data_access/). The CPC Unified

536 Gauge-Based Analysis of Global Daily Precipitation dataset is available at

537 https://climatedataguide.ucar.edu/climate-data/cpc-unified-gauge-based-analysis-glob

538 al-daily-precipitation.   ECMWF   reanalysis   data   are   accessible   via

539 http://apps.ecmwf.int/datasets/data/interim-full-daily/. MODIS data and CloudSat data

540 are   available   at   https://modis.gsfc.nasa.gov/data/   and

541 http://www.cloudsat.cira.colostate.edu/, respectively. Ground-based observations of

542 precipitation amount, visibility, precipitable water, and CAPE from Fujian Province

543 can be requested from the Chinese Meteorological Administration's National

544 Meteorological Information Center (http://cdc.cmic.cn and http://data.cma.cn/).

545   **Acknowledgements**

546   This study was supported by the Ministry of Science and Technology of China

547   (2013CB955804), the Fundamental Research Funds for the Central Universities of

548   China (312231103), State Key Laboratory of Earth Surface Processes and Resource

549   Ecology (2015-TDZD-090), and NOAA (NA15NWS4680011). We would like to

550   thank the NASA Global Modeling and Assimilation Office

551   (https://gmao.gsfc.nasa.gov/reanalysis/MERRA-2/data_access/) and the Goddard

552   Space Flight Center Distributed Active Archive Center for their help in accessing

553   MERRA-2 inst3_2d_gas_Nx: 2d, 3-Hourly, Instantaneous, Single-Level, Assimilation,

554   Aerosol Optical Depth Analysis Version 5.12.4 data. We would also like to thank the

555   staff at the National Center for Atmospheric Research responsible for creating the

556   "The Climate Data Guide: CPC Unified Gauge-Based Analysis of Global Daily

557   Precipitation"

558   (https://climatedataguide.ucar.edu/climate-data/cpc-unified-gauge-based-analysis-glob

559   al-daily-precipitation). Thanks   also   go   to   the   NOAA   NOMADS

560   (https://nomads.ncdc.noaa.gov/)   for   GFS   data

561   (https://nomads.ncdc.noaa.gov/data/gfs4/),   the   NOAA   NCDC

562   (https://www.ncdc.noaa.gov/data-access/model-data/model-datasets/global-ensemble-

563   forecast-system-gefs) for GEFS reforecast data, and the NWS CPC for data

564   downloading software (http://www.cpc.ncep.noaa.gov/products/wesley/get_gfs.html).

565   We   acknowledge   the   Chinese   Meteorological   Administration's   National

566   Meteorological Information Center (http://cdc.cmic.cn and http://data.cma.cn/), the

567   European   Centre   for   Medium-Range   Weather   Forecasts   (ECMWF)

568   (http://www.ecmwf.int/),   the   NASA   Goddard   Space   Flight   Center

569   (https://modis.gsfc.nasa.gov/data/), and the CloudSat Data Processing Center

570   (http://www.cloudsat.cira.colostate.edu/) for providing the various datasets used in the

571   study.

572   We would also like to thank Drs. Shrinivas Moorthi, and Jun Wang from NOAA,

573   Sarah Lu from State University of New York, Albany, Dr. Seoung-Soo Lee from the

574   University of Maryland, and Drs. Duoying Ji and Lanning Wang from Beijing Normal

575   University for their discussions regarding this study. We especially appreciate the help

576   given by Dr. Jongil Han in understanding the GFS/GEFS models and data products,

577   and the guidance provided by Dr. Hye-Lim Yoo. We also greatly appreciate the

578   valuable comments from the anonymous reviewers.

579

580

References

Ackerman, A. S., Toon, O. B. , Stevens, D. E., Heymsfield, A. J., Ramanathan, V., and Welton, E. J.: Reduction of tropical cloudiness by soot, Science, 288(5468), 1042–1047, doi:10.1126/science.288.5468.1042, 2000.

Albrecht, B. A.: Aerosols, cloud microphysics, and fractional cloudiness, Science, 245(4923), 1227–1230, doi:10.1126/science.245.4923.1227, 1989.

Andreae, M. O., Rosenfeld, D., Artaxo, P., Costa, A. A., Frank, G. P., Longo, K. M., and Silva-Dias, M. A. F.: Smoking rain clouds over the Amazon, Science, 303(5662), 1337–1342, doi:10.1126/science.1092779, 2004.

Appel, B. R., Tokiwa, Y., Hsu, J., Kothny, E. L., and Hahn, E.: Visibility as related to atmospheric aerosol constituents, Atmos. Environ., 19, 1525–1534, doi: 10.1016/j.bbr.2011.03.031, 1985.

Arakawa, A., and Schubert, W. H.: Interaction of a cumulus cloud ensemble with the large-scale environment. Part I. J. Atmos. Sci., 31, 674–701, doi:10.1175/1520-0469(1974)031<0674:IOACCE>2.0.CO;2, 1974.

Bell, T., Rosenfeld, D., Kim, K., Yoo, J., Lee, M., and Hahnenberger, M.: Midweek increase in U.S. summer rain and storm heights suggests air pollution invigorates rainstorms, J. Geophys. Res. Atmos., 113, D02209, doi:10.1029/2007JD008623, 2008.

Carrió, G. G., Cotton, W. R., and Cheng, W. Y. Y.: Urban growth and aerosol effects on convection over Houston. Part I: The August 2000 case, Atmos. Res., 96(4), 560–574, doi: 10.1016/j.atmosres.2010.01.005, 2010.

Charlson, R. J.: Atmospheric visibility related to aerosol mass concentration: Review, Environ. Sci. Technol., 3, 913–918, doi:10.1021/es60033a002, 1969.

Chin, M., Ginoux, P., Kinne, S., Torres, O., Holben, B., Duncan, B. N., Martin, R. V., Logan, J., Higurashi, A., and Nakajima, T.: Tropospheric aerosol optical thickness from the GOCART model and comparisons with satellite and Sun photometer measurements, J. Atmos. Phys., 59, 461–483, doi:10.1175/1520-0469(2002)059<0461:TAOTFT>2.0.CO;2, 2002.

da Silva, A., Colarco, P. R., Darmenoy, A. S., Buchard-Marchant, V., Randles, C. A., and Gupta, P.: An overview of the GEOS-5 Aerosol Reanalysis, American Geophysical Union, Fall Meeting

2011, abstract #A52D-09, San Francisco, CA, USA, 2011.

Fan, J. W., Rosenfeld, D., Yang, Y., Zhao, C., Leung, L. R., and Li, Z.: Substantial contribution of anthropogenic air pollution to catastrophic floods in Southwest China, Geophys. Res. Lett., 42(14), 6066–6075, doi:10.1002/2015GL064479, 2015.

Fan, J. W., Wang, Y., Rosenfeld, D., and Liu, X.: Review of aerosol–cloud interactions: mechanisms, significance, and challenges, J. Atmos. Sci., 73(11), 4221–4252, doi:10.1175/JAS-D-16-0037.1, 2016.

GCWM Branch, EMC: The GFS atmospheric model. NCEP Office Note 442, 14 pp., available at: http://wwwt.emc.ncep.noaa.gov/officenotes, 2003.

Grell, G. A.: Prognostic evaluation of assumptions used by cumulus parameterizations, Mon. Wea. Rev., 121, 764–787, doi:10.1175/1520-0493(1993)121<0764:PEOAUB>2.0.CO;2, 1993.

Gryspeerdt, E., Stier, P. and Partridge, D.G.: Satellite observations of cloud regime development: The role of aerosol processes, Atmos. Chem. Phys., 14(3), 1141–1158, doi:10.5194/acp-14-1141-2014, 2014a.

Gryspeerdt, E., Stier, P. and Partridge, D.G.: Links between satellite-retrieved aerosol and precipitation, Atmos. Chem. Phys., 14(18), 9677–9694, doi:10.5194/acp-14-9677-2014, 2014b.

Han, J., and Pan, H. L.: Revision of convection and vertical diffusion schemes in the NCEP Global Forecast System, Wea. Forecasting, 26, 520–533, doi:10.1175/WAF-D-10-05038.1, 2011.

Han, J., Witek, M. L., Teixeira, J., Sun, R., Pan, H. L., Fletcher, J. K., and Bretherton, C. S.: Implementation in the NCEP GFS of a Hybrid Eddy-Diffusivity Mass-Flux (EDMF) boundary layer parameterization with dissipative heating and modified stable boundary layer mixing, Wea. Forecasting, 31(1), 341–352, doi:10.1175/WAF-D-15-0053.1, 2016.

Hong, S. Y., and Pan, H. L.: Nonlocal boundary layer vertical diffusion in a medium-range forecast model, Mon. Wea. Rev., 124, 2322–2339, doi:10.1175/1520-0493(1996)124<2322:NBLVDI>2.0.CO;2, 1996.

Intergovernmental Panel on Climate Change: Climate Change 2013: The Physical Science Basis, in Contribution of Working Group I to the Fifth Assessment Report of the Intergovernmental Panel on Climate Change, Cambridge Univ. Press, Cambridge, U. K., 2013.

Jiang, H., Xue, H., Teller, A., Feingold, G., and Levin, Z.: Aerosol effects on the lifetime of shallow cumulus, Geophys. Res. Lett., 33(14), doi:10.1029/2006gl026024, 2006.

Jiang, M., Li, Z., Wan, B., and Cribb, M.: Impact of aerosols on precipitation from deep convective clouds in eastern China, J. Geophys. Res. Atmos., 121(16), 9607–9620, doi:10.1002/2015JD024246, 2016.

Kanamitsu, M.: Description of the NMC Global Data Assimilation and Forecast System, Wea. Forecasting, 4(3), 335–342, doi:10.1175/1520-0434(1989)004<0335:DOTNGD>2.0.CO;2, 1989.

Kaufman, Y., Koren, I., Remer, L., Rosenfeld, D., and Rudich, Y.: The effect of smoke, dust, and pollution aerosol on shallow cloud development over the Atlantic Ocean, Proc. Nat. Acad. Sci. USA, 102(32), 11,207–11,212, doi:10.1073/pnas.0505191102, 2005.

Khain, A, Benmoshe, N., and Pokrovsky, A.: Factors determining the impact of aerosols on surface precipitation from clouds: An attempt at classification, J. Atmos. Sci., 65(5), 1721–1748, doi:10.1175/2007JAS2515.1, 2008.

Koren, I., Kaufman, Y. J., Rosenfeld, D., Remer, L. A., and Rudich, Y.: Aerosol invigoration and restructuring of Atlantic convective clouds, Geophys. Res. Lett., 32(14), doi: 10.1029/2005gl023187, 2005.

Koren, I., Martins, J. V., Remer, L. A., and Afargan, H.: Smoke invigoration versus inhibition of clouds over the Amazon, Science, 321(5891), 946–949, doi:10.1126/science.1159185, 2008.

Li, Z., Niu, F., Fan, J., Liu, Y., Rosenfeld, D., and Ding, Y.: Long-term impacts of aerosols on the vertical development of clouds and precipitation, Nat. Geosci., 4(12), 888–894, doi:10.1038/ngeo1313, 2011.

Li, Z., Lau, W. K.-M., Ramanathan, V., Wu, G., Ding, Y., Manoj, M. G., Liu, J., Qian, Y., Li, J., Zhou, T., Fan, J., Rosenfeld, D., Ming, Y., Wang, Y., Huang, J., Wang, B., Xu, X., Lee, S.-S., Cribb, M., Zhang, F., Yang, X., Zhao, C., Takemura, T., Wang, K., Xia, X., Yin, Y., Zhang, H., Guo, J., Zhai, P. M., Sugimoto, N., Babu, S. S., and Brasseur, G. P.: Aerosol and monsoon climate interactions over Asia, Rev. Geophys., 54(4), 866–929, doi:10.1002/2015RG000500, 2016.

Lin, Y., and Zhao, C.: Trends of precipitation of different intensity in China, Acta Scientiarum

Naturalium Universitatis Pekinensis, 45, 995–1002, 2009.

Lin, J. C., Matsui, T., Pielke, R. A., and Kummerow, C.: Effects of biomass-burning-derived aerosols on precipitation and clouds in the Amazon Basin: a satellite-based empirical study, J. Geophys. Res. Atmos., 111(D19), doi:10.1029/2005jd006884, 2006.

Moorthi, S., Pan, H. L., and Caplan, P.: Changes to the 2001 NCEP operational MRF/AVN global analysis/forecast system, NWS Technical Procedures Bulletin, 484, available online at www. nws.noaa.gov/om/tpb/484.htm, 2001.

Niu, F., and Li, Z.: Systematic variations of cloud top temperature and precipitation rate with aerosols over the global tropics, Atmos. Chem. Phys., 12(18), 8491–8498, doi:10.5194/acp-12-8491-2012, 2012.

Pan, H. L., and Wu, W. S.: Implementing a mass flux convective parameterization package for the NMC Medium-Range Forecast model, NMC Office Note 409, 40 pp, 1995.

Peng, J., Li, Z., Zhang, H., Liu, J., and Cribb, M. C.: Systematic changes in cloud radiative forcing with aerosol loading for deep clouds in the tropics, J. Atmos. Sci., 73, 231–249, doi:10.1175/JAS-D-15-0080.1, 2016.

Randles, C. A., da Silva, A. M., Buchard, V., Darmenoy, A., Colarco, P. R., Aquila, V., Bian, H., Nowottnick, E. P., Pan, X., Smirnov, A., Yu, H., and Govindaraju, R.: The MERRA-2 Aerosol Assimilation, NASA Tech. Rep. Series on Global Modeling and Data Assimilation, NASA TM—2016-104606, 45, 156 pp, 2016.

Rienecker, M. M., Suarez, M. J., Gelaro, R., Todling, R., Bacmeister, J., Liu, E., Bosilovich, M. G., Schubert, S. D., Takacs, L., Kim, G. K., Bloom, S., Chen, J., Collins, D., Conaty, A., da Silva, A., Gu, W., Joiner, J., Koster, R. D., Lucchesi, R., Molod, A., Owens, T., Pawson, S., Pegion, P., Redder, C. R., Reichle, R., Robertson, F. R., Ruddick, A. G., Sienkiewicz, M., and Woollen, J.: MERRA: NASA's Modern-Era Retrospective Analysis for Research and Applications, J. Climate, 24(14), 3624–3648, doi:10.1175/JCLI-D-11-00015.1, 2011.

Rosenfeld, D.: Suppression of rain and snow by urban and industrial air pollution, Science, 287(5459), 1793–1796, doi:10.1126/science.287.5459.1793, 2000.

Rosenfeld, D., Dai, J., Yu, X., Yao, Z., Xu, X., Yang, X., and Du, C.: Inverse relations between amounts of air pollution and orographic precipitation, Science, 315, 1396–1398,

697 doi:10.1126/science.1137949, 2007.

698 Rosenfeld, D., Lohmann, U., Raga, G.B., Dowd, C. D. O., Kulmala, M., Fuzzi, S., Reissell, A.,

699  and Andreae, M. O.: Flood or drought: How do aerosols affect precipitation?, Science,

700  321(5894), 1309–1313, doi:10.1126/science.1160606, 2008.

701 Sela, J.: Implementation of the sigma pressure hybrid coordinate into GFS; NCEP Office, Note #

702  461, available at http://www.emc.ncep.noaa.gov/officenotes/FullTOC.html#2000, 2009.

703 Sundqvist, H., Berge, E., and Kristjansson, J. E.: Condensation and cloud parameterization studies

704  with a mesoscale numerical weather prediction model, Mon. Wea. Rev., 117, 1641–1657,

705  doi:10.1175/1520-0493(1989)117<1641:CACPSW>2.0.CO%3B2, 1989.

706 Tao, W. K., Chen, J. P., Li, Z., Wang, C., and Zhang, C.: Impact of aerosols on convective clouds

707  and precipitation, Rev. Geophys., 50(2), doi:10.1029/2011rg000369, 2012.

708 Tapiador, F. J., Turk, F. J., Petersen, W., Hou, A. Y., Garcá-Ortega, E., Machado, L. A., Angelis, C.

709  F., Salio, P., Kidd, C., Huffman, G. J., and De Castro, M.: Global precipitation measurement:

710  Methods, datasets and applications, Atmos. Res., 104, 70–97,

711  https://doi.org/10.1016/j.atmosres.2011.10.021, 2012.

712 Troen, I., and Mahrt, L.: A simple model of the atmospheric boundary layer: Sensitivity to surface

713  evaporation, Bound.-Layer Meteor., 37, 129–148, doi: 10.1007/BF00122760, 1986.

714 Twomey, S. A., Piepgrass, M., and Wolfe, T. L.: An assessment of the impact of pollution on

715  global cloud albedo, Tellus B, 36(5), 356–366, doi:10.1111/j.1600-0889.1984.tb00254.x,

716  1984.

717 van den Heever, S. C., Stephens, G. L., and Wood, N. B.: Aerosol indirect effects on tropical

718  convection characteristics under conditions of radiative–convective equilibrium, J. Atmos.

719  Sci., 68(4), 699–718, doi: http://dx.doi.org/10.1175/2010JAS3603.1, 2011.

720 Xie, P. P., Yatagai, A., Chen, M. Y., Hayasaka, T., Fukushima, Y., Liu, C. M., and Yang, S.: A

721  gauge-based analysis of daily precipitation over East Asia, J. Hydrometeorol., 8(3), 607–626,

722  doi:10.1175/Jhm583.1, 2007.

723 Xue, H., and Feingold, G.: Large-eddy simulations of trade wind cumuli: investigation of aerosol

724  indirect effects, J. Atmos. Sci., 63(6), 1605–1622, doi:10.1175/JAS3706.1, 2006.

725 Yang, F. L., Pan., H. L., Krueger, S. K., Moorthi, S., and Lord, S. J.: Evaluation of the NCEP

726   Global Forecast System at the ARM SGP site, Mon. Wea. Rev., 134(12), 3668–3690,

727   doi:10.1175/MWR3264.1, 2006.

728 Yang, X., and Li, Z.: Increases in thunderstorm activity and relationships with air pollution in

729   southeast China, J. Geophys. Res. Atmos., 119, 1835–1844, doi:10.1002/2013JD021224,

730   2014.

731 Yang, X., Ferrat, M., and Li, Z.: New evidence of orographic precipitation suppression by aerosols

732   in central China, Meteor. Atmos. Phys., 119, 17–29, doi:10.1007/s00703-012-0221-9, 2013.

733 Yoo, H., and Li, Z.: Evaluation of cloud properties in the NOAA/NCEP global forecast system

734   using multiple satellite products, Clim. Dyn., 39, 2769–2787,

735   doi:10.1007/s00382-012-1430-0, 2012.

736 Yoo, H., Li, Z., Hou, Y.-T, Lord, S., Weng, F., and Barker, H. W.: Diagnosis and testing of

737   low-level cloud parameterizations for the NCEP/GFS model satellite and ground-based

738   measurements, Clim. Dyn., 41, 1595–1613, doi:10.1007/s00382-013-1884-8, 2013.

739 Zhang, J., Reid., J., and Holben, B.: An analysis of potential cloud artifacts in MODIS over ocean

740   aerosol optical thickness products, Geophys. Res. Lett., 32, L15803,

741   doi:10.1029/2005GL023254, 2005.

742 Zhao, Q. Y., and Carr, F. H.: A prognostic cloud scheme for operational NWP models, Mon. Wea.

743   Rev., 125, 1931–1953, doi:10.1175/1520-0493(1997)125<1931:APCSFO>2.0.CO;2, 1997.

744

745   **Table 1.** Definitions of warm- and cold-base mixed-phase clouds and liquid clouds.

	Cloud-base temperature (^{o}C)	Cloud-top temperature (^{o}C)
Deep mixed-phase clouds with warm bases	> 15	< -4
Shallow mixed-phase clouds with cold bases	0–15	< -4
Liquid clouds	> 0	> 0

746

747

748   **Table 2.** Contingency table.

Observed / Forecast	Observed yes	Observed no
Forecast yes	Hits	False alarms
Forecast no	Misses	Correct negatives

749

750

751   **Table 3.** Correlation coefficients from linear regressions of visibility and different rain

752   amount types for all seasons.

Rain rate / Season	Light rain	Moderate rain	Heavy rain	Very heavy rain	Rain amount
Spring	0.48*	0.51*	0.48*	0.17	0.40*
Summer	0.08	-0.16	-0.28	-0.41*	-0.38*
Autumn	0.31	0.18	0.26	-0.22	0.11
Winter	0.55*	0.26	0.26	0.27	0.29

753   * Values with an asterisk represent data at a confidence level greater than 95%.

754

755 **Table 4.** Correlation coefficients from linear regressions of visibility and different

756 occurrence frequencies of rain amount type for all seasons.

Rain rate / Season	Light rain	Moderate rain	Heavy rain	Very heavy rain	Rain amount
Spring	0.61*	0.51*	0.38*	0.08	0.67*
Summer	0.23	-0.13	-0.26	-0.44*	-0.04
Autumn	0.52*	0.18	0.25	-0.10	0.45*
Winter	0.55*	0.22	0.20	-0.05	0.49*

757 * Values with an asterisk represent data at a confidence level greater than 95%.

758

759

760

761

762

763

764

765
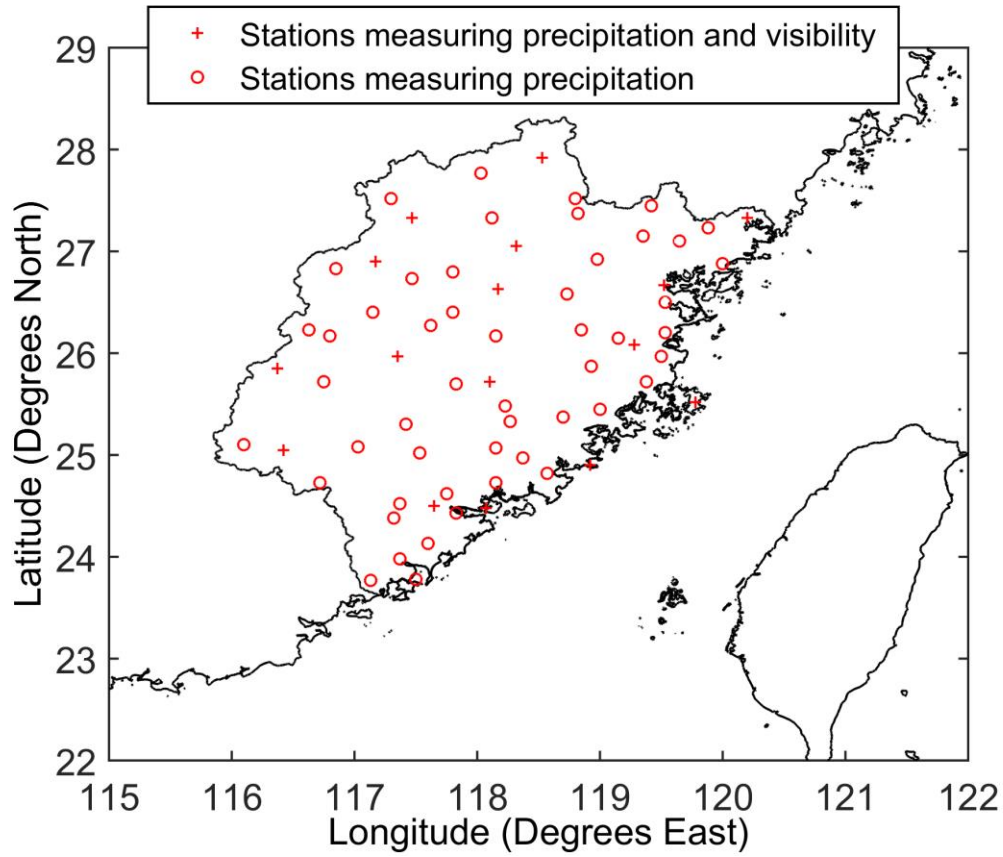
766

767 **Fig. 1.** Locations of 67 stations measuring precipitation in Fujian Province. Plus
768 symbols show the locations of the 16 stations where visibility measurements are also
769 made. This figure was plotted using the equidistant cylindrical projection.

770
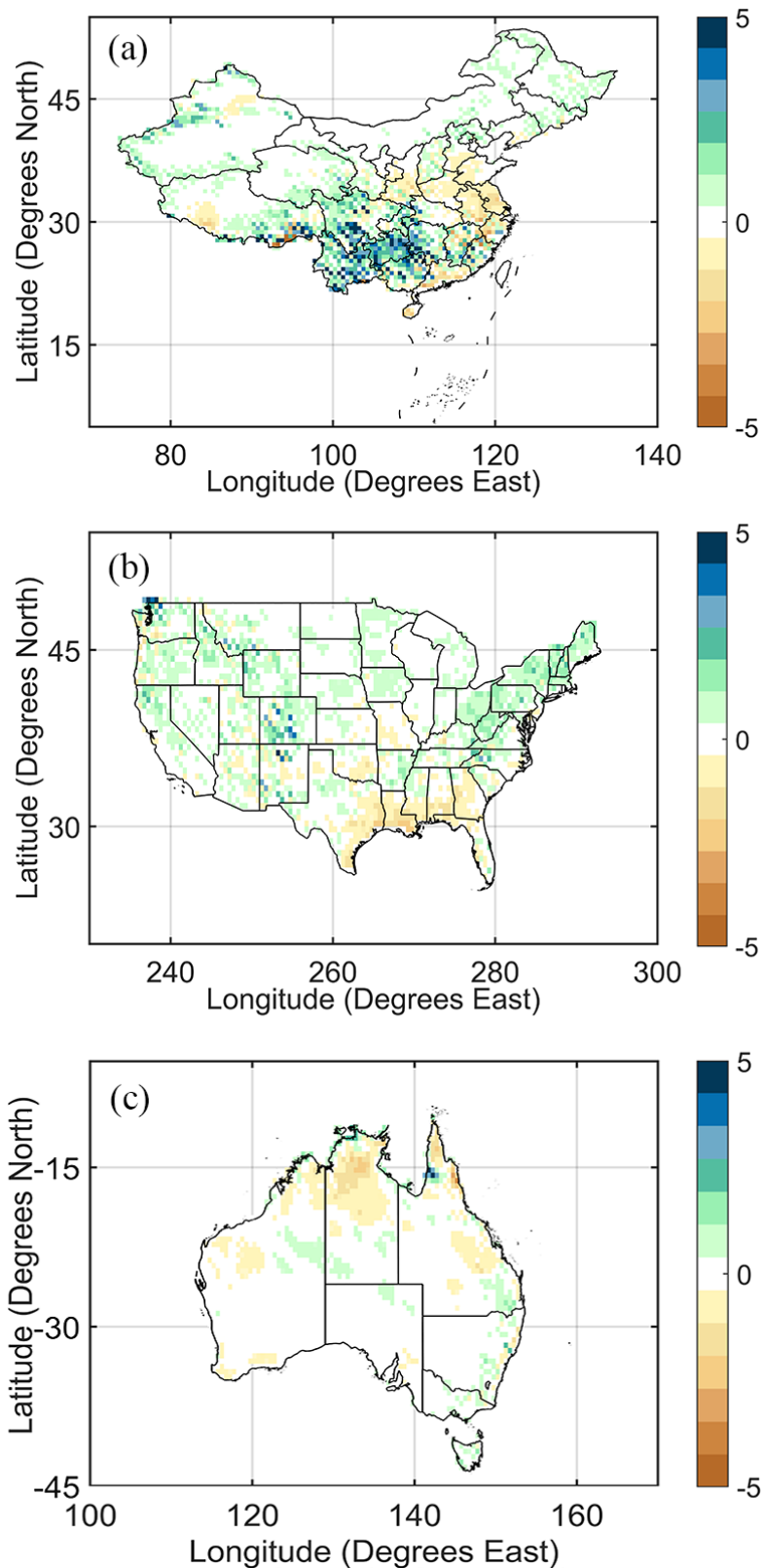
Fig. 2. Annual mean precipitation differences (in mm d^{-1}) between the GFS model
forecast and the CPC analysis in three countries: (a) China, (b) the contiguous U.S.,
and (c) Australia. Data are from the year 2015. This figure was plotted using the
equidistant cylindrical projection.
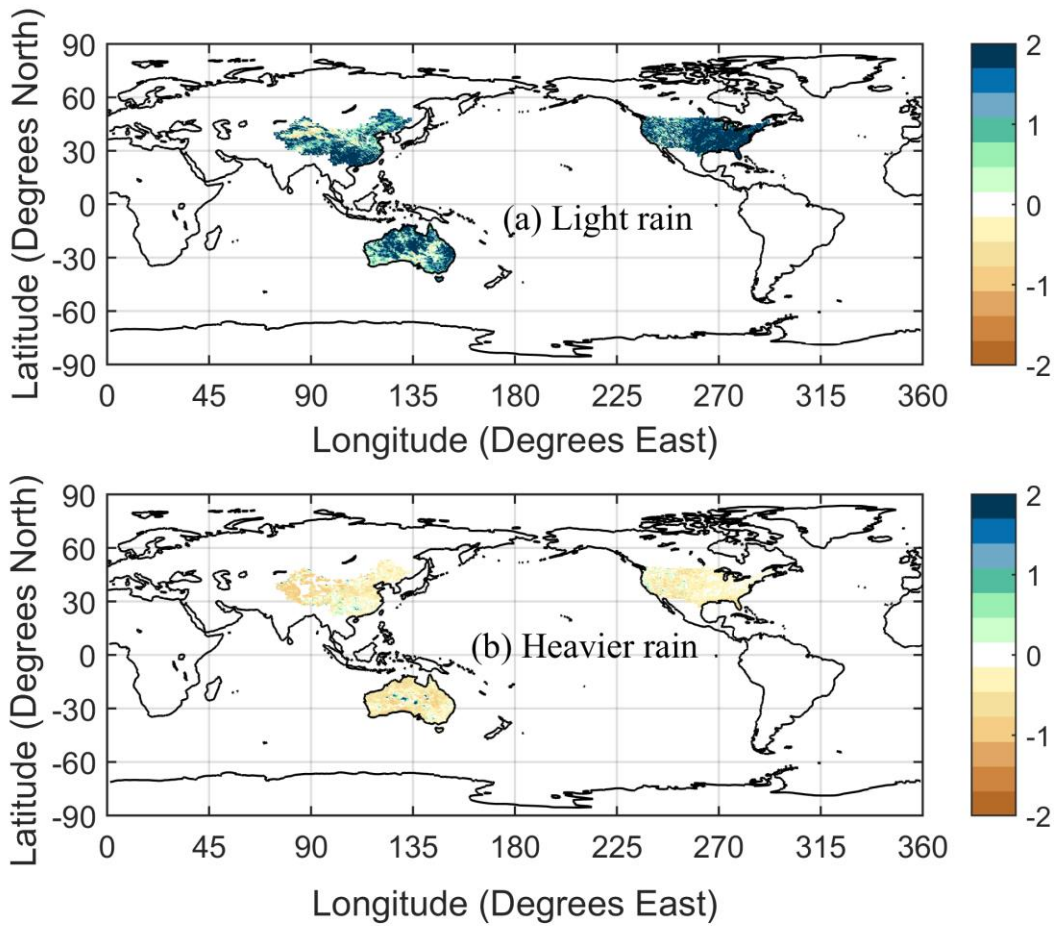
Fig. 3. Annual mean relative difference (in mm d^{-1}) between forecast and observed precipitation for (a) light rain (< 10 mm d^{-1}) and (b) heavier rain (> 10 mm d^{-1}). Data are from the year 2015. This figure was plotted using the equidistant cylindrical projection.
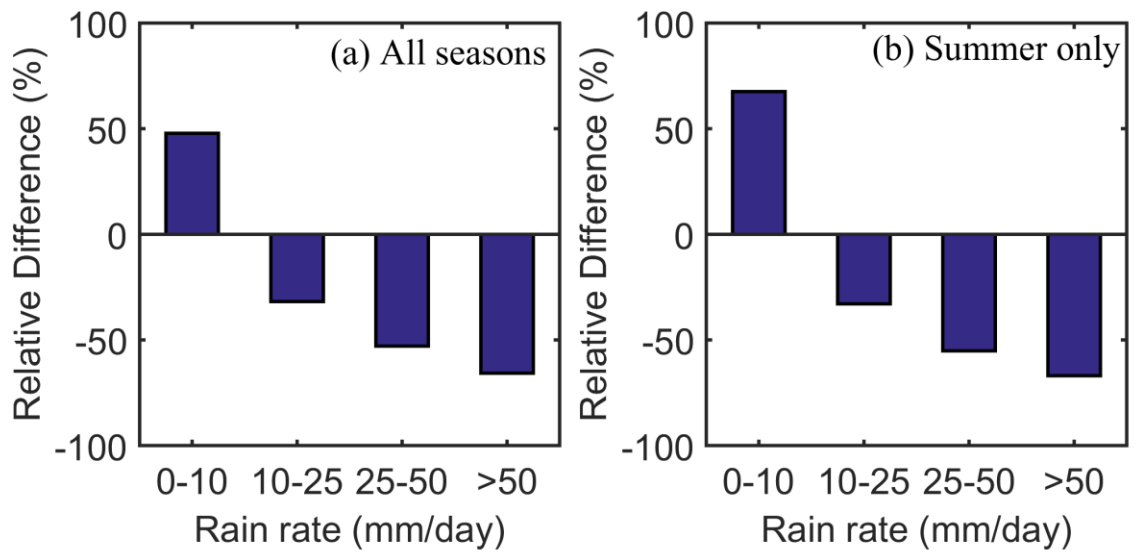
781
782 **Fig. 4.** Mean relative difference in precipitation between forecast and observed daily
783 light (< 10 mm d^{-1}), moderate (10–25 mm d^{-1}), heavy (25–50 mm d^{-1}), and very heavy
784 (> 50 mm d^{-1}) rain amounts for (a) all seasons and (b) summer only. Data are from the
785 year 2015 and from the three countries considered in the study.
786

787
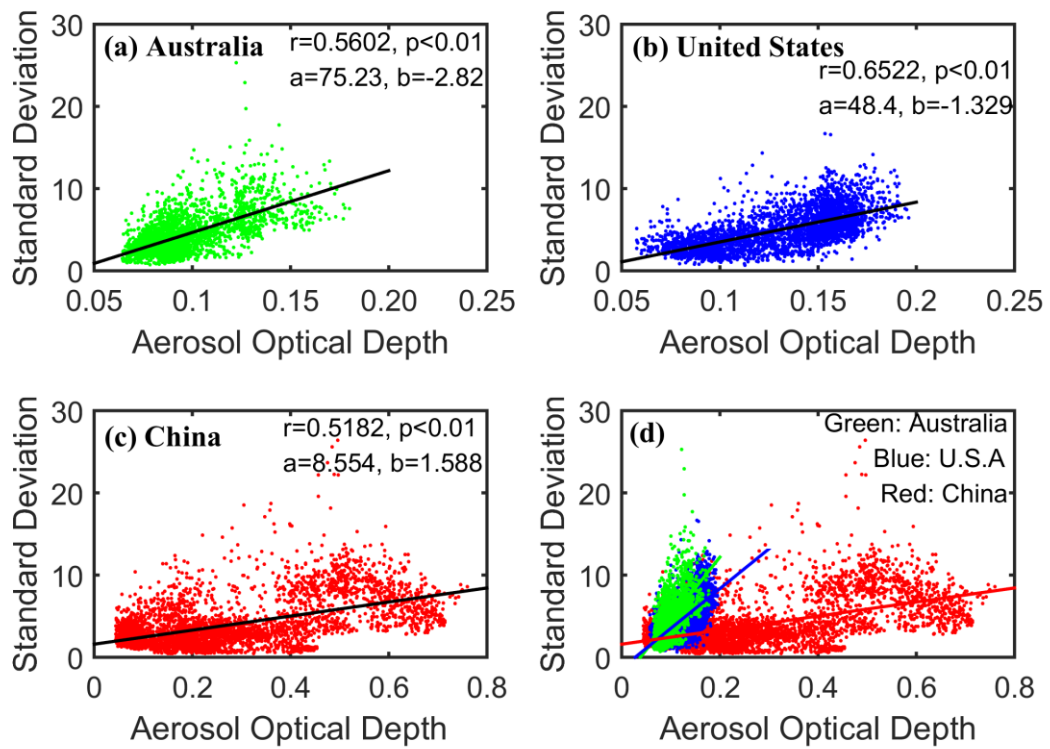
Fig. 5. Standard deviations of the daily precipitation difference as a function of
aerosol optical depth for (a) Australia (green points), (b) the United States (blue
points), (c) China (red points), and (d) all three countries. Data are from the year 2015.
The slopes (a) and y-intercepts (b) of the best-fit lines through the data in (a) to (c) are
given, as well as the correlation coefficients (r).

793
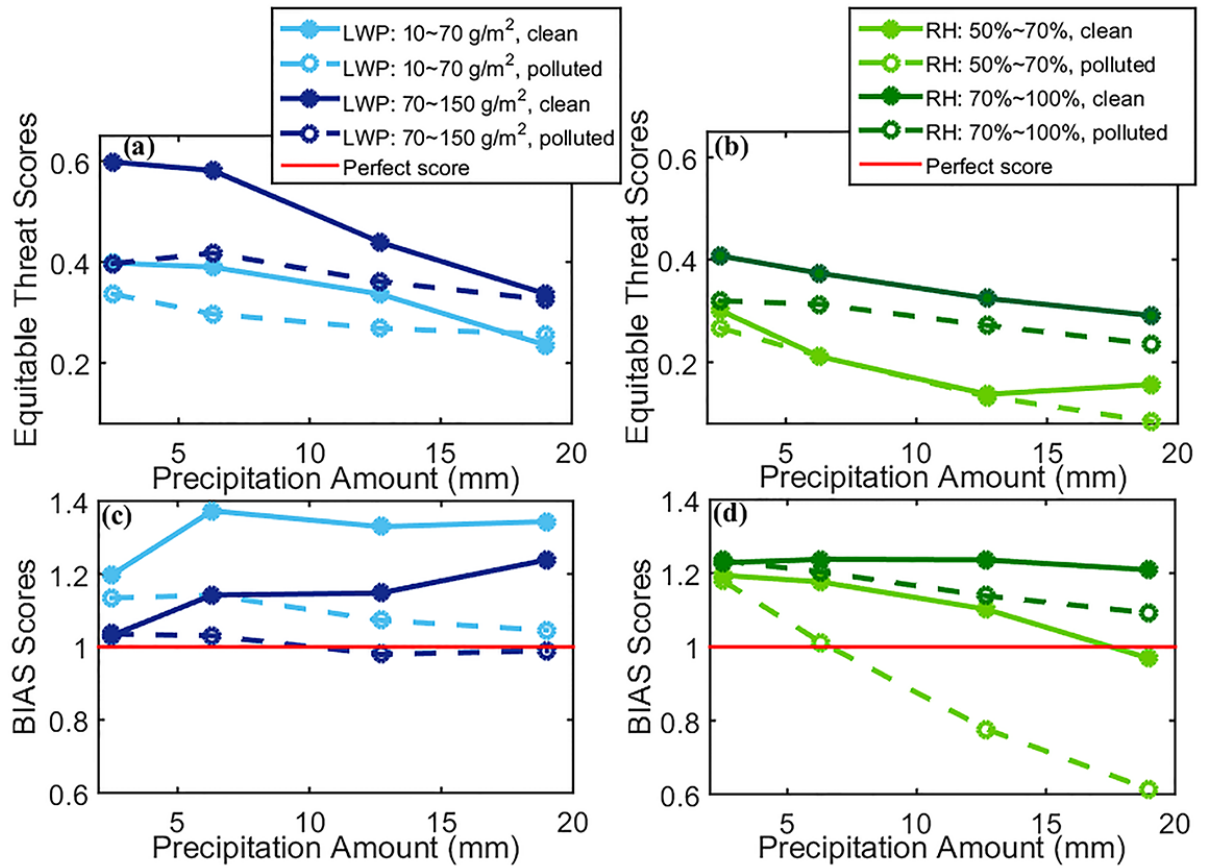
Fig. 6. Equitable threat scores (a, b) and bias (BIAS) scores (c, d) as a function of precipitation amount for fixed ranges of liquid water path (LWP; a, c) and relative humidity (RH; b, d) under clean and polluted conditions. The LWP is divided into two categories: 10–70 g m^{-2} (light blue) and 70–150 g m^{-2} (dark blue). Data are from August 2015 in the U.S, China, and Australia. The RH is divided into two categories: 50–70% (light green) and 70–100% (dark green). Data are from year 2015. For a given LWP or RH condition, the top and bottom one-third of AOD values are defined as polluted and clean subsets of data, respectively. The solid lines represent the clean scenario and the dotted lines represent the polluted scenario. The horizontal red lines in (c) and (d) represent perfect scores.
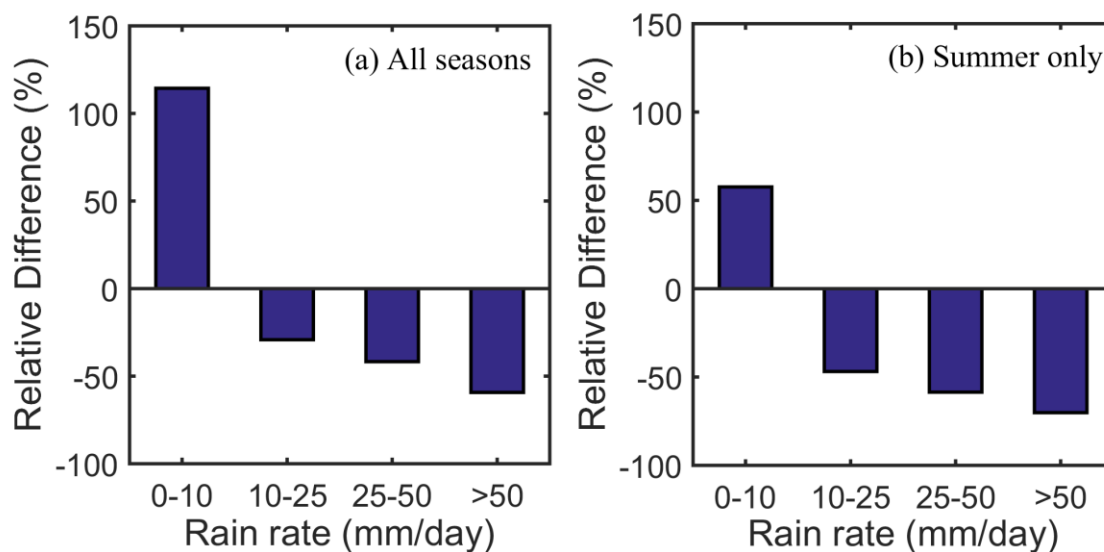
811 **Fig. 7.** Mean relative precipitation differences between forecast and observed daily
812 light (< 10 mm d^{-1}), moderate (10–25 mm d^{-1}), heavy (25–50 mm d^{-1}), and very heavy
813 (> 50 mm d^{-1}) rain amounts for (a) all seasons and (b) summer only in Fujian
814 Province, China. Data are from 1985–2010.

810

815

816
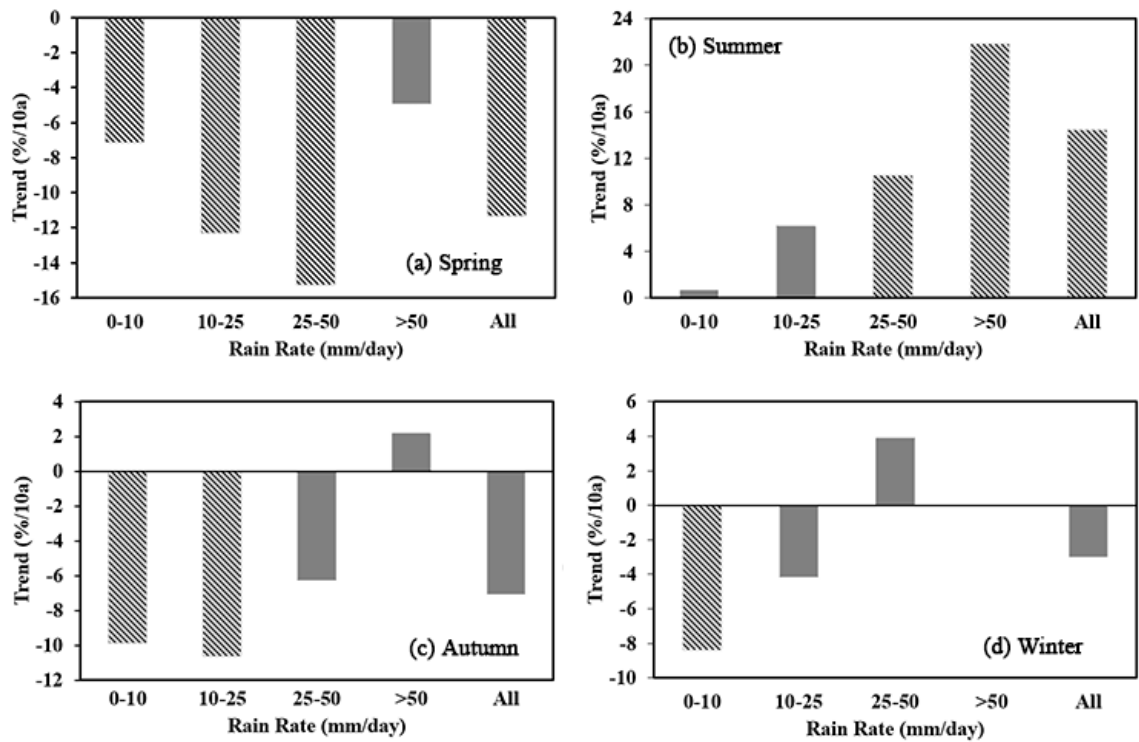
817

818 **Fig. 8.** Trends (percent change per decade) in mean daily light rain (< 10 mm d^{-1}),
819 moderate rain (10–25 mm d^{-1}), heavy rain (25–50 mm d^{-1}), very heavy rain (> 50 mm
820 d^{-1}), and total rain amounts for (a) spring, (b) summer, (c) autumn, and (d) winter in
821 Fujian Province, China. Data are from 1980–2009. Cross-hatched bars represent data
822 at a confidence level greater than 95%.
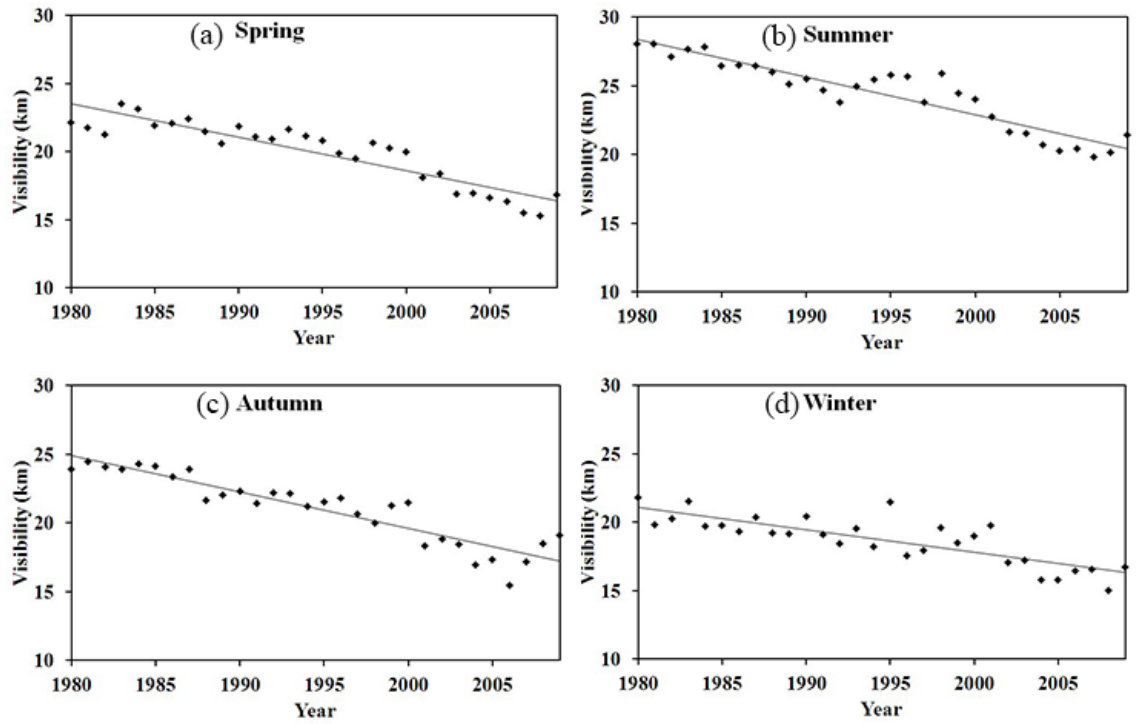
823

824 **Fig. 9.** Annual mean visibilities in (a) spring, (b) summer, (c) autumn, and (d) winter

825 in Fujian Province, China. Data are from 1980–2009. Least squares regression lines at

826 the 95% confidence level are shown.

827
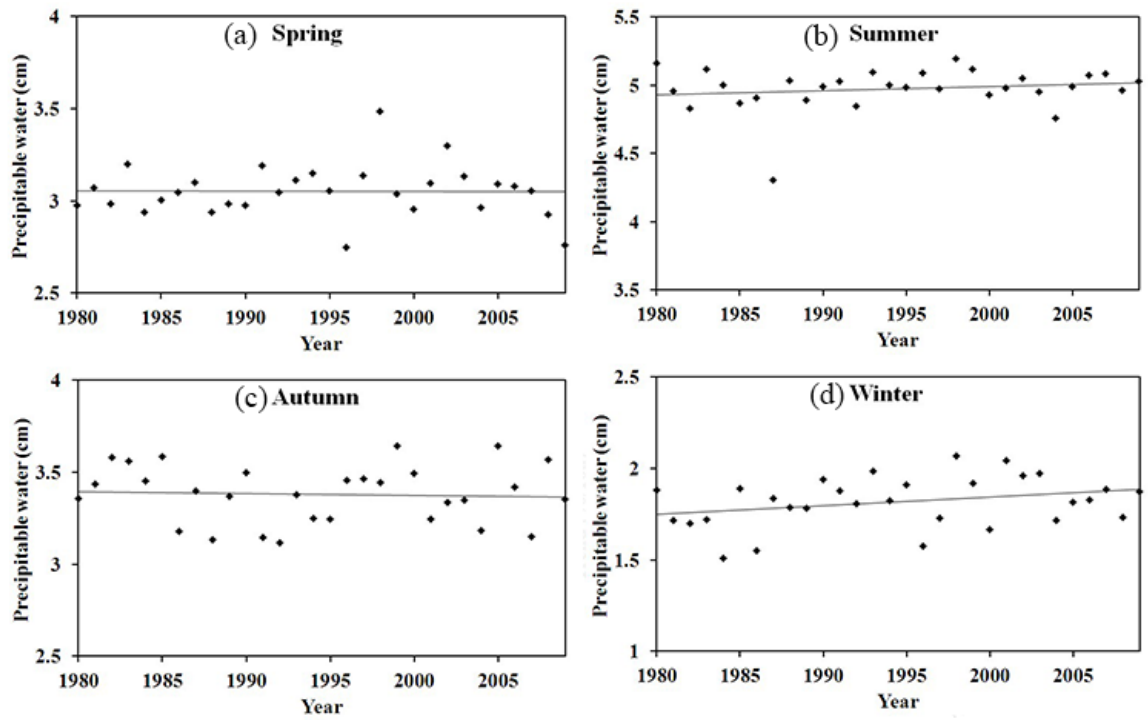
828

829 **Fig. 10.** Same as Fig. 9, except for precipitable water vapor.

830

831
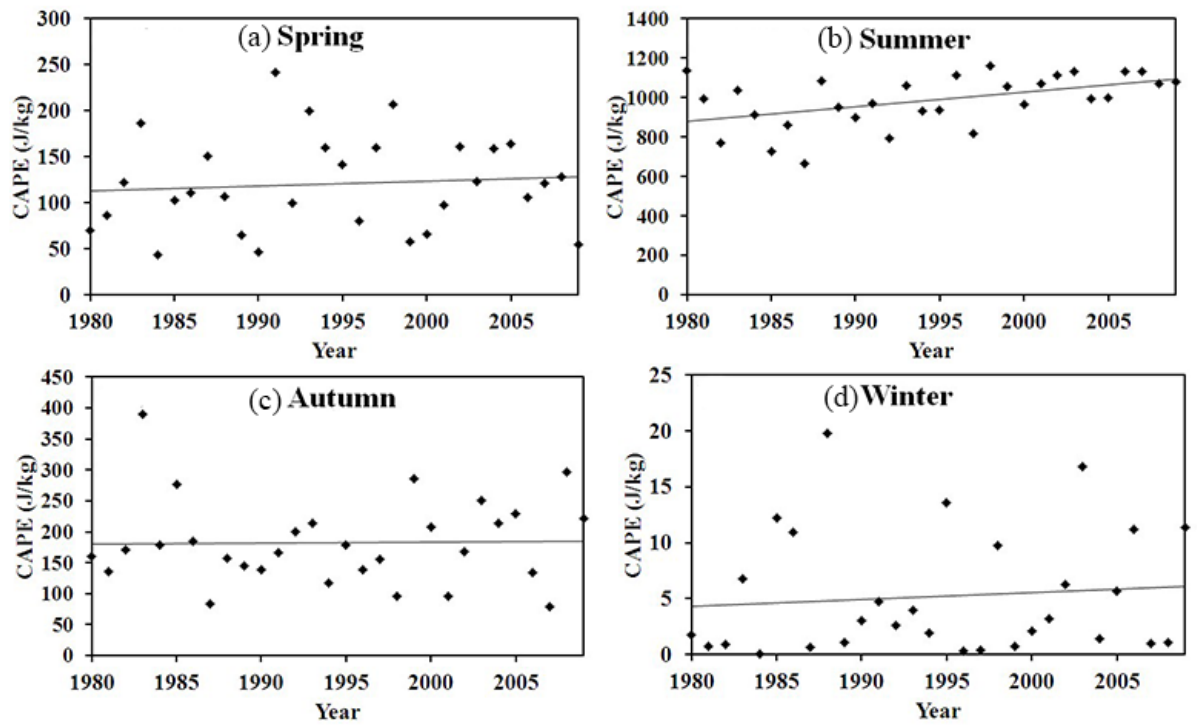
832

833   **Fig. 11.** Same as Fig. 9, except for convective available potential energy (CAPE).

834

835

836
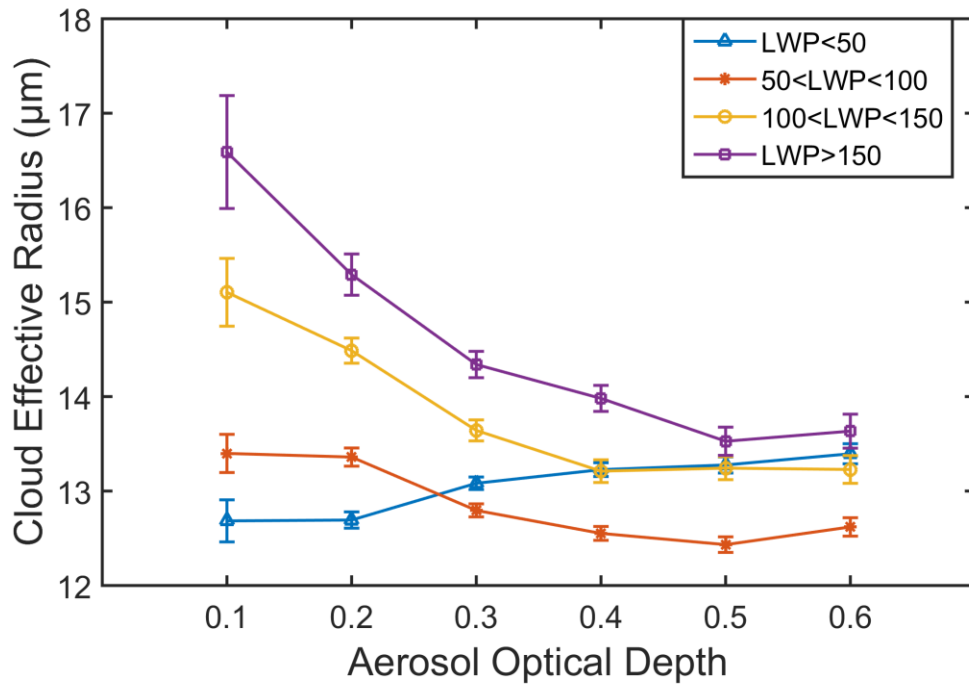
Fig. 12. Cloud effective radius as a function of aerosol optical depth for liquid clouds
(clouds with top temperatures greater than 273 K) in Fujian Province, China. Blue
triangles represent cases where the liquid water path (LWP) is less than 50 g m^{-2},
orange stars represent LWPs between 50 g m^{-2} and 100 g m^{-2}, yellow circles represent
LWPs between 100 g m^{-2} and 150 g m^{-2}, and purple squares represent LWPs greater
than 150 g m^{-2}. Error bars represent one standard error. Data are from 2003–2012.

843
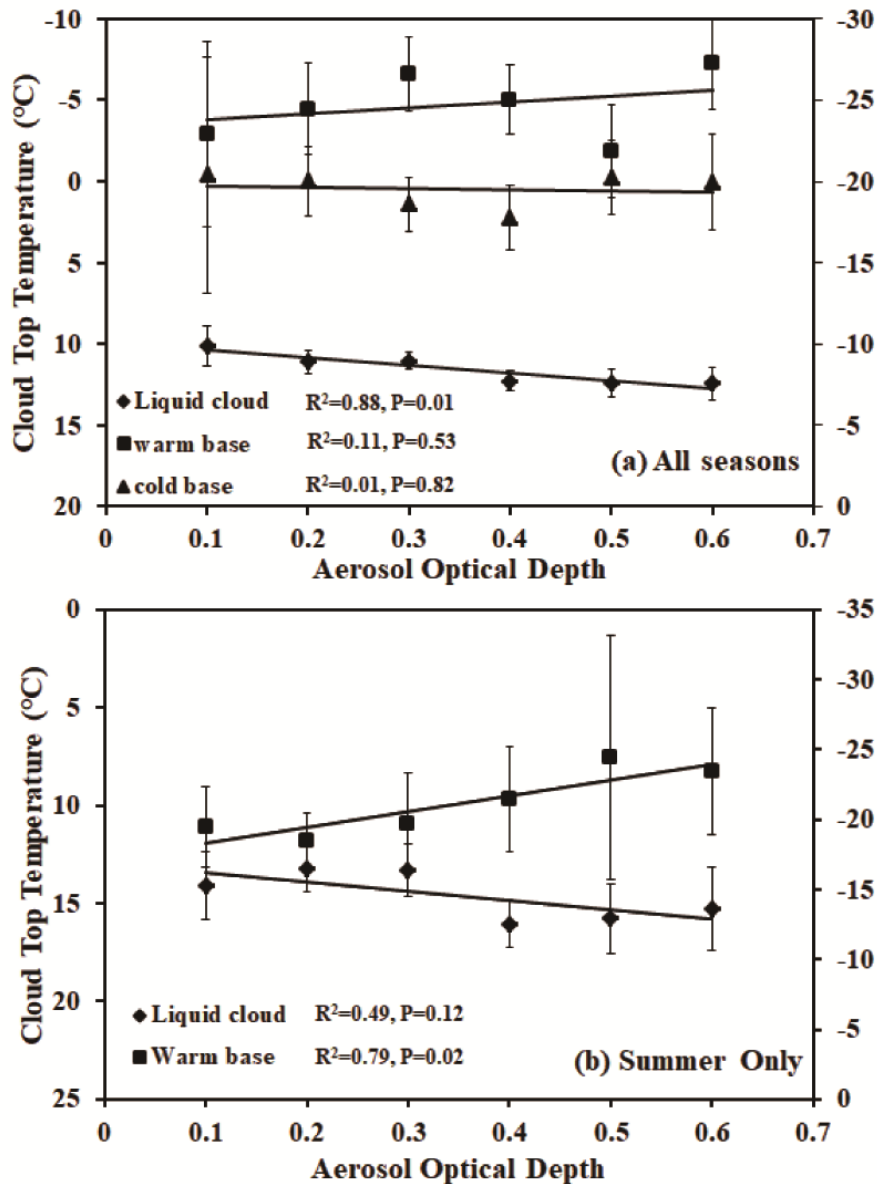
Fig. 13. Cloud-top temperature as a function of aerosol optical depth for (a) liquid,
warm-base mixed-phase, and cold-base mixed-phase clouds in all seasons, and (b)
liquid and warm-base mixed-phase clouds in summer in Fujian Province, China.
Diamonds represent liquid clouds, squares represent warm-base mixed-phase clouds,
and triangles represent cold-base mixed-phase clouds. Right-hand ordinates are for
warm-base and cold-base mixed-phase clouds. Data are from 2006–2010.
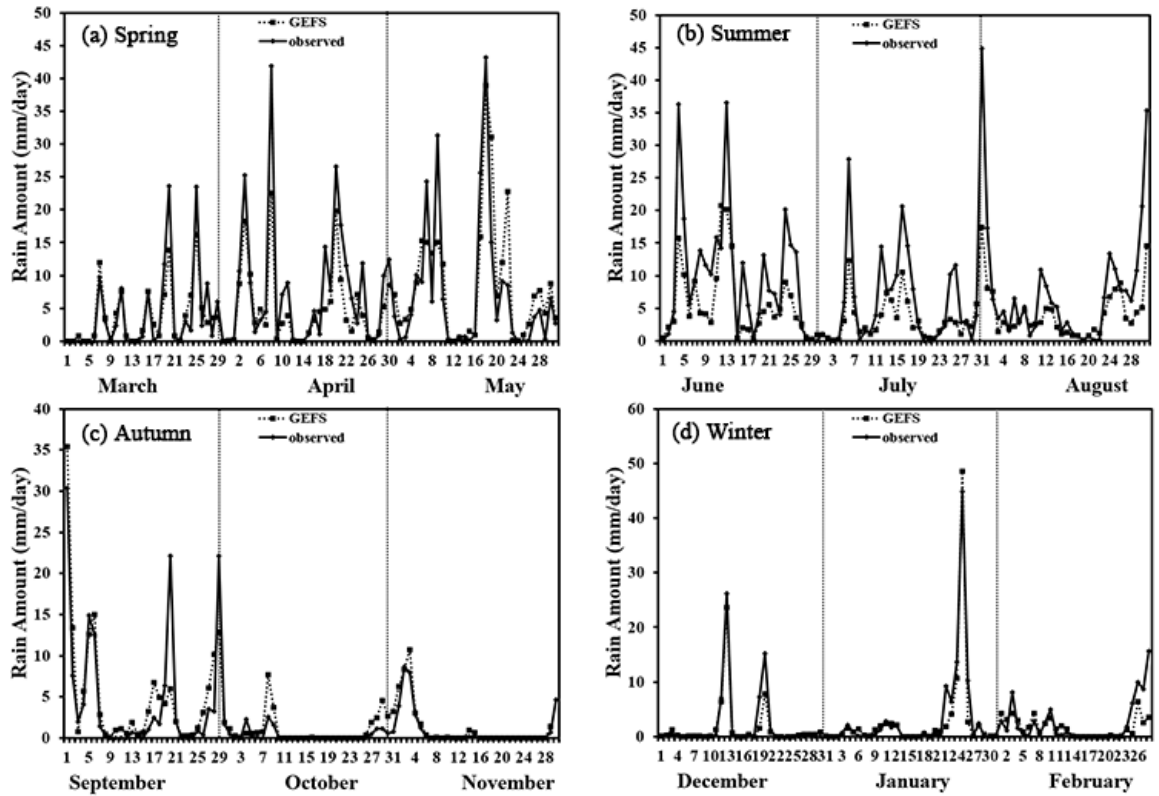
850
851 **Fig. 14.** Time series of regionally-averaged daily rainfall amount in Fujian Province,
852 China in (a) spring, (b) summer, (c) autumn, and (d) winter. Dotted lines represent
853 rainfall forecasts from the Global Ensemble Forecast System and solid lines represent
854 rainfall measurements from gauge-based observations. Data are from 2001.